



ORIGINAL RESEARCH

A wearable circulator-like circularly polarised antenna for full-duplex wireless body area network applications

 Ajeet Thakur¹  | Ashwani Sharma¹ | Ignacio J. Garcia Zuazola² 
¹Electrical Engineering Department, Indian Institute of Technology Ropar, Punjab, India

²School of Computing and Digital Media, London Metropolitan University, London, UK

Correspondence

 Ignacio J. Garcia Zuazola.
Email: i.garciazuazola@londonmet.ac.uk

Funding information

SERB, Department of Science & Technology, Government of India, Grant/Award Number: CRG/2022/007257

Abstract

A circulator-like high gain, unidirectional, dual circularly polarised (DCP) wearable antenna with a low specific absorption rate of 0.088 W/kg for 5.8 GHz industrial, scientific, and medical (ISM) band (5.725 – 5.875 GHz) full-duplex wireless body area network (WBAN) applications is proposed. The DCP full-duplexing is achieved by a closed-loop feedback structure between its orthogonal-ports with enhanced axial ratio (AR) bandwidth and good impedance matching. The antenna is backed with a 7×7 electromagnetic bandgap array that allows for improved directionality, AR and isolation between the ports. The cross-polarisation level above 17 dB is attained in the broadside direction, in both the E-plane and the H-plane, indicating good polarisation discrimination. Since the total power at each respective port is maintained and not halved (-3 dB) with the measured port isolation of ~ 28 dB in real scenarios (with the potential evidence of ~ 34 dB) within the ISM band, that leads to a circulator-like antenna, meaning that a typically cascaded circulator/duplexer can be relieved and leave to the digital processing any self-interference challenge of full duplex systems through digital cancellation techniques, which alleviates the overall costs of RF hardware and eases integration. Even though dual linear polarization as well as DCP can be supported, the closed-loop feedback structure uses a port as Tx (RHCP) and the other one as Rx (LHCP) simultaneously with enhanced AR bandwidth. Without this structure, it would require a circulator/duplexer for DCP full-duplex operation and the associated added insertion losses and/or $\frac{1}{2}$ power (if duplexers) for operation, together with a polarisation misalignment problem that is undesired in wearable WBAN applications.

KEYWORDS

antenna testing, antennas, microwave antennas

1 | INTRODUCTION

With the rapidly growing popularity of wireless body area network (WBAN) systems, wearable antennas are common in healthcare, the armed forces, sports, and firefighting applications and are preferred to be compact, lightweight, mechanically robust and flexible so that they can be easily embedded within the clothing or wearable electronic devices. As wearable antennas function next to the lossy human body, it is essential to consider the effect of human body loading while designing such antennas. At the same time, the specific absorption rate

(SAR) that determines the level of EM radiation exposing the human body needs to be controlled to ensure the user's safety. According to FCC standards, SAR must be lower than the average 1.6 W/kg per gram of tissue [1].

For the communication transfer of information between on-body antennas and off-body terminals more effectively, a full-duplex system allowing simultaneous reception (Rx) and transmission (Tx) is essential [2]. Conventionally, the Rx/Tx is accomplished by an RF switch connecting the Rx/Tx module to a single port antenna using a time division duplexing scheme. However, the use of this time sharing is at the expense

This is an open access article under the terms of the [Creative Commons Attribution-NonCommercial-NoDerivs](https://creativecommons.org/licenses/by-nc-nd/4.0/) License, which permits use and distribution in any medium, provided the original work is properly cited, the use is non-commercial and no modifications or adaptations are made.

© 2024 The Author(s). *IET Microwaves, Antennas & Propagation* published by John Wiley & Sons Ltd on behalf of The Institution of Engineering and Technology.

of system complexity, system efficiency and throughput. In contrast, a dual-port antenna with each port directly linked to the Rx and the Tx modules is a better solution [3–5]. But, dual-port antennas [6, 7] are far from the full-duplex Rx/Tx operation because of the frequency-sharing scheme where each port operates different frequencies and has dissimilar radiation characteristics. That results to an inefficient frequency spectrum usage. Also, linearly polarised (LP) antennas [2, 5, 8] are prone to polarisation mismatch due to changeable gestures and human body motion [9, 10]. As a solution, dual circularly polarised (DCP) full-duplex antennas are promising candidates for WBAN applications owing to their polarisation (orientation) flexibility, better resource utilisation than time and frequency sharing, resistant to Faraday's effect, and multipath suppression capability [11].

In the literature, several DCP antennas are extensively investigated so far in refs. [12–23]. To attain DCP characteristics, several schemes are utilised, for instance, a combination of L-shaped strips (LSSs) and inverted LSSs in refs. [12, 19], two asymmetric microstrip line exciting a U-shaped slot in ref. [13], inverted-L grounded strips with additional three strips in ref. [14], and offset feeding technique in ref. [17]. To further realise high isolation between two DCP ports, a mirrored F-shaped defected ground structure (DGS) and three grounded stubs are utilised in ref. [17]. A MIMO DCP antenna presented in ref. [19] is designed on a flexible substrate for wearable applications; however, this antenna exhibits a bidirectional radiation pattern that is unwelcome in WBAN applications. Various other designs obtaining unidirectional patterns are reported in the literature [15, 16, 18, 20–23] whose directionality is controlled by techniques using full ground, metal reflector etc. All these designs exhibit DCP operation and are either made on rigid substrates or on complex non-planar 3D geometries, hence unattractive for wearable applications. Thus, a DCP full-duplex planar antenna achieving a unidirectional pattern and designed on a flexible substrate for wearable application is sought in this work.

Further, to minimise the SAR, numerous methods have been utilised in the literature such as the use of perfect electric conductors (PECs), ferrite sheets, electromagnetic band gaps (EBGs) etc. The use of PEC [24] is discouraged due to its out-of-phase-reflection characteristics resulting into substantially lowered efficiency. The use of ferrite sheets [25, 26] or increasing the separation between the user's body and the antenna [27] leads to bulky and costly systems. Other methods for SAR reduction involve backing the wearable antenna with periodically loaded structures such as electromagnetic bandgap (EBG), artificial magnetic conductors and high impedance surfaces [28–30]. These periodic structures enhance antenna gain, reducing surface waves and emitted radiations pointing towards the user's body, limiting the SAR, and hence ensuring the safety of the user [31, 32]. Furthermore, using this surface wave suppression capability of EBGs enhanced isolation between antenna ports is feasible [33]. EBGs will therefore be exploited to increase the impedance and axial ratio (AR) bandwidths of a DCP wearable antenna for full-duplex applications.

In this work, a circulator-like high gain, unidirectional, DCP wearable antenna with low SAR for the 5.8 GHz industrial, scientific, and medical (ISM) band (5.725 – 5.875 GHz) full-duplex WBAN application is proposed. The DCP full-duplexing is achieved by a closed-loop feedback structure between the orthogonal ports with enhanced AR bandwidth and good impedance matching. Aided by a 7×7 EBG array, it allows for improved directionality, AR and isolation between the ports, which leads to a circulator-like antenna behaviour.

The remaining of the manuscript is detailed as next. Section 2 describes the proposed design and analysis. The simulated results and measurement are presented in Section 3 and Section 4, respectively. SAR performance and comparative analysis are described in Section 5 and Section 6, respectively, and conclusions are drawn in Section 7.

2 | PROPOSED DESIGN AND ANALYSIS

This section presents a detailed analysis of the antenna design principles and the step-by-step development of EBG, elucidating the methodical steps taken to achieve the final layout design.

2.1 | Antenna configuration

The proposed circulator-like circularly polarised (CP) antenna is designed using high-frequency structure simulator (HFSS) v. 22, and Figure 1 portrays the final layout. The concluding dimensions are detailed as follows: $L_{sub} = 61.04$, $l = 5.275$, $l_d = 4.5$, $l_g = 20.2$, $l_n = 11.825$, $l_s = 2.75$, $l_1 = 7$, $l_2 = 3.75$, $l_3 = 16.4$, $l_4 = 2.5$, $l_5 = 4.2$, $l_6 = 6.28$, $w = 0.5$, $w_f = 1.8$, $w_g = 9.45$, $w_{sub} = 36$, $w_1 = 0.8$, $w_2 = 0.75$, $p_1 = 8.68$, $p_2 = 8.4$, $p_3 = 6$, $a = 2.25$, $b = 0.51$, $h_1 = 1.57$, $h_2 = 3$, and $h_3 = 0.508$ (units: mm).

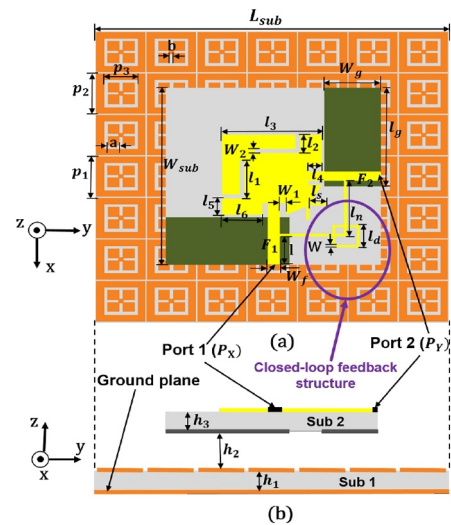


FIGURE 1 EBG-integrated antenna topology (a) top view. (b) Front view. EBG, electromagnetic bandgap.

The circulator-like CP antenna consists of two layers of substrates, sub 1 and sub 2, with thicknesses $h_1 = 1.57$ mm and $h_3 = 0.508$ mm, respectively. Both the layers make use of the RT/duroid 5880, a semi-flexible substrate having relative permittivity and loss tangent, respectively, as $\epsilon_r = 2.2$ and $\tan \delta = 0.0009$. The antenna comprises a monopole-type structure on the top layer of Sub 2 with a patch having a pair of inverted L-shaped slots (i_1, i_2), two orthogonal strips (S_1, S_2) protruding at the far end edges of the patch, a closed-loop feedback structure comprising a square slot (S_q) connected between the orthogonal feed lines (F_1, F_2), and two ground planes (G_1, G_2) as depicted in Figure 2c. The antenna is fed using two orthogonal 50 Ω -microstrip lines F_1 and F_2 , which are terminated to antenna ports P_X and P_Y , respectively, as shown in Figure 1.

The features of monopole include DCP and bidirectional radiation characteristics, which exhibits low AR, low gain and poor port isolation. Therefore, an EBG periodic structure is used below the radiating patch to enhance AR, gain, isolation between Tx and Rx ports, and reduce the backward radiation for SAR improvement. The tailored EBG with the 7×7 array of slotted square patch unit cells laid on Sub 1 is shown in Figure 1. The evolution of this structure is presented subsequently.

2.2 | Design principle and evolution

For the design, a dual orthogonal-port square patch antenna termed as Ant. 1 evolves up to the proposed design, Ant. 4. They are presented in Figure 2. The Ant. 1 comprises a square patch fed with two orthogonal 50 Ω -microstrip feed lines. To evaluate the performance of full-duplex operation, only one port is excited as the transmitter since the other port is simultaneously acting as the receiver. Therefore, during the evaluation, the Port 1 (P_X) is excited and Port 2 (P_Y) is terminated with a matched load. The simulated S-parameters, port isolation, AR, and absolute gains are plotted in Figure 3.

As observed in Figure 3, the Ant. 1 shows poor port isolation and gain and LP behaviour. Moreover, it operates at 6.3 GHz which needs to be shifted down to the desired frequency of 5.8 GHz. This requires an increment in the antenna's effective electrical length and is accomplished by chamfering (C_1, C_2) the square patch at the lower edge, protruding S_1, S_2 and inserting i_1, i_2 as illustrated by Ant. 2 in Figure 2b. The Ant. 2 achieves CP around 5.52 GHz, as illustrated by the AR

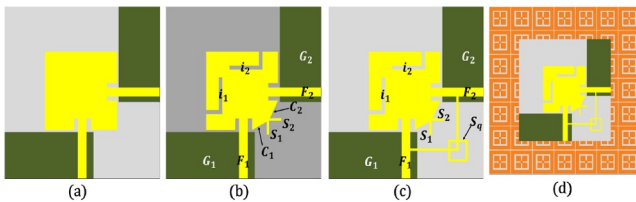


FIGURE 2 Proposed EBG-integrated antenna's evolution (a) Ant. 1. (b) Ant. 2. (c) Ant. 3. (d) Ant. 4. EBG, electromagnetic bandgap.

results shown in Figure 3c. Theoretically, CP can be achieved by generating two orthogonal electric field vectors (E_x and E_y) with equal amplitude and 90° phase difference. Chamfering (C_1, C_2) the square patch, protruding S_1, S_2 and inserting i_1, i_2 contribute to attaining the identical E_x and E_y components with a phase difference close to 90° around 5.52 GHz as shown in Figure 4a,b. Moreover, the S_{11} result of Ant. 2 in Figure 3a indicates potential frequency down shifting; however, the impedance matching requires further improvement.

For this, S_q is protruded at the lower edge of the patch which is directly connected to F_1 and F_2 , thereby forming a closed-loop feedback structure as illustrated by Ant. 3 in Figure 2c. This results in improved impedance matching with enhanced impedance and AR bandwidths ranging from 5.47–6.15 GHz and 5.56–5.96 GHz, respectively, as depicted in Figure 3a,c, hence covering the entire 5.8 GHz ISM band. The inductance generated by the closed-loop feedback structure suppresses some of the capacitance produced by Ant. 2, which is responsible for improved impedance matching and enhanced impedance bandwidth. Additionally, the closed-loop

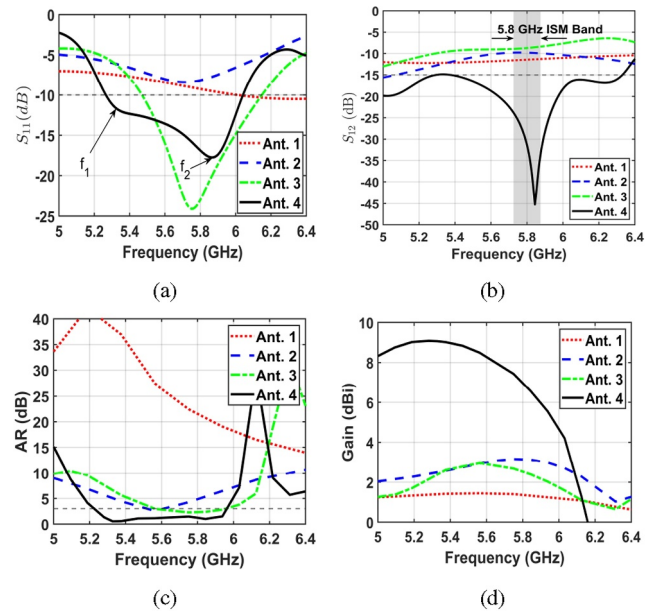


FIGURE 3 Simulated (a) S_{11} . (b) S_{12} . (c) AR. (d) Absolute gain for Antennas 1–4. AR, axial ratio.

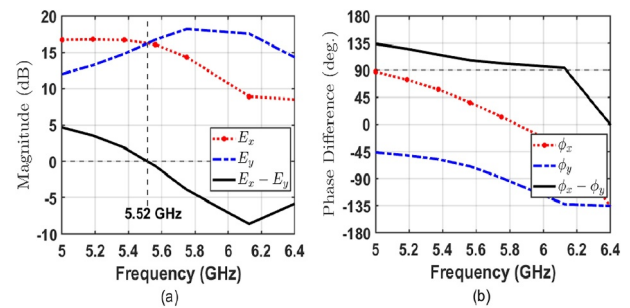


FIGURE 4 Simulated (a) magnitude. (b) Phase of E_x and E_y components of Ant. 2.

feedback structure contributes in balancing the difference of the amplitudes and the phases of two electric field vectors (E_x and E_y) in the desired band, that is, 5.725 – 5.875 GHz as illustrated in Figures 5a–b. The magnitude and phase both vary very smoothly, implying a wider AR bandwidth.

Thus, the closed-loop feedback structure tunes impedance matching, achieves DCP behaviour in the band of interest and customises the polarisation of the antenna, which is illustrated in Section 3.1 through a parametric analysis. However, as shown in Figure 3b, the poor port isolation of around 9 dB is still present between the two ports. This can be observed in the current distribution plot of Figure 6a where the area around the feed line of P_Y is marked to show the coupled intensity.

Finally, Ant. 3 is placed above the 7×7 EBG array to form Ant. 4 as shown in Figure 2d. To emphasise, the proposed EBG-integrated antenna exhibits a wider impedance bandwidth as displayed in Figure 3a having a range of 5.26 – 6.1 GHz. It is due to the additional matching offered by EBG (f_2) other than the monopole itself (f_1) to generate a wider bandwidth. This is further evidenced in Section 3.1 through parametric analysis. As presented in Figure 3b for the Ant. 4, the simulated isolation between ports for the ISM band seemed encouraging. Also, the 3 dB AR bandwidth for Ant.4, as presented in Figure 3c, ranges from 5.21 – 5.96 GHz. Thus, the impedance and AR bandwidths are overlapped in the range of 5.54 – 5.96 GHz with encouraging port isolation for the targeted band. The EBG structure's ability to suppress the propagation of surface waves is the reason for better isolation between ports P_X and P_Y [33]. This can be observed by the current distribution plotted in Figure 6b where the coupled intensity around P_Y is marked by a dashed rectangular area

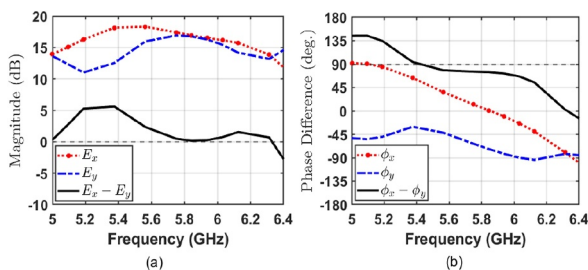


FIGURE 5 Simulated (a) magnitude. (b) Phase of E_x and E_y components of Ant. 3.

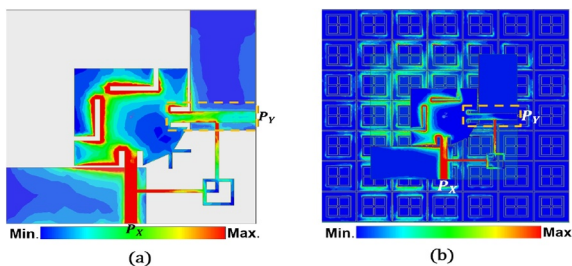


FIGURE 6 Simulated current distribution at 5.8 GHz while P_X is excited (a) Ant. 3. (b) Ant. 4.

which is very low compared to the Ant. 3, Figure 6a. Moreover, the improvement in AR is also observable in Figure 3c for the antenna completed with EBG (Ant. 4).

A high gain enhancement is achieved by loading the EBG structure in Ant. 4 as evident from Figure 3d. The broadside gain in $\theta = 0^\circ$ direction is 4.82 dBi increased by the proposed Ant. 4 as compared to Ant. 3 at the band of interest. The unidirectional radiation increases the gain as portrayed by the patterns plotted in Figure 7, and therefore lower SAR is anticipated for the proposed Ant. 4 design in proximity to a highly dielectric lossy human body.

2.3 | EBG design and evolution

The EBG unit cell is evolved from a square patch as EBG 1 to the final design EBG 3 as shown in Figure 8.

The desired frequency can be determined using $f = \frac{1}{2\pi\sqrt{LC}}$ [34], where 'C' and 'L' are, respectively, the equivalent capacitance and inductance associated with the EBG unit cell. The

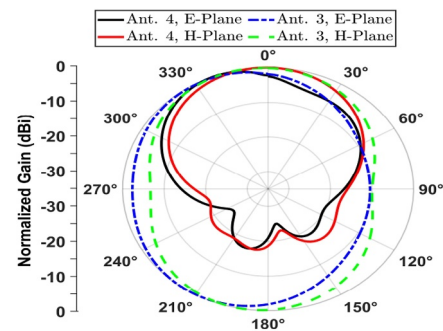


FIGURE 7 Simulated normalised gain pattern, at 5.8 GHz, when P_X is excited.

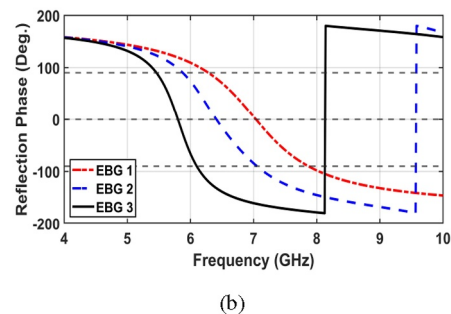
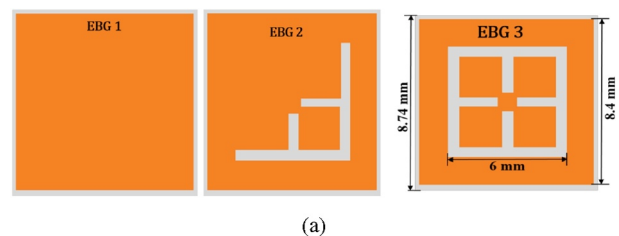


FIGURE 8 EBG unit cell (a) Evolution process. (b) Simulated reflection phases. EBG, electromagnetic bandgap.

equation makes it clear that changes in ‘C’ or ‘L’ have an impact on the resonant frequency. Both parameters decrease the frequency as they are increased, but capacitance also reduces the bandwidth. Hence, increasing inductance by using a thick substrate is preferable over increasing the capacitance to maintain a wide bandwidth [35]. The reflection phase characteristics and dispersion of these cells are investigated using HFSS.

First, EBG 1 uses a square patch as shown in Figure 8a and its reflection phase is plotted in Figure 8b. The 0° reflection phase occurs at 7.03 GHz for EBG 1. Next, the EBG 2 in Figure 8a is evolved by inserting a pair of T-shaped slots on the square patch which leads to a frequency shift, in the 0° reflection phase, down to 6.4 GHz as observed from Figure 8b. This is due to the fact that the slots increase the current path, thereby increasing the inductance and, hence, drifting the resonant frequency towards the lower side. The reflection phase is further shifted down to obtain the desired frequency of 5.8 GHz by EBG 3 which is formed by inserting two more identical T-shaped slots on EBG 2. This also decreases the $\pm 90^\circ$ reflection phase bandwidth slightly due to the extra capacitance created by slots between the edges. Nevertheless, the EBG 3 still covers the desired frequency range.

The frequency shifting phenomenon is examined by the surface current plotted in Figure 9a for 5.8 GHz of the EBG 3. It is apparent that the current flows more along the slots; therefore, the 0° reflection phase and bandwidth of EBG 3 unit cell can both be controlled by the inserted slots. Also, it is clear from Figure 9b that 0° reflection phase occurs at 5.8 GHz and that the $\pm 90^\circ$ bandwidth lies between 5.46 and 6.10 GHz. A dispersion diagram presented in Figure 9c corroborates the frequency range, hence covering the band of interest.

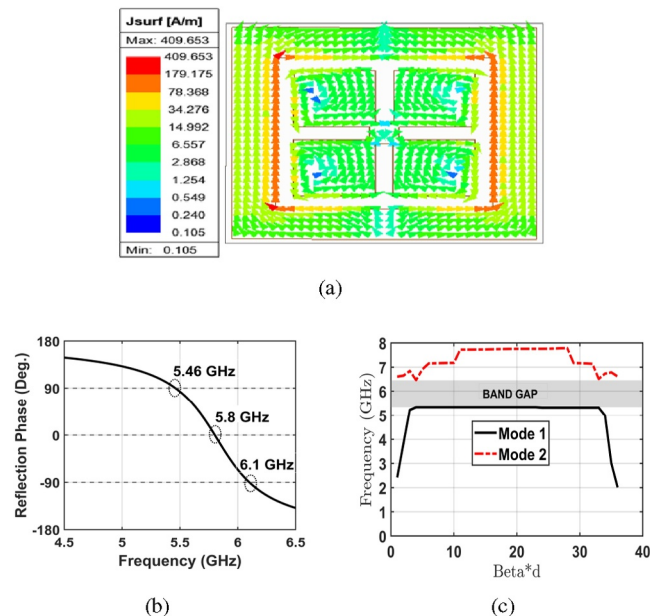


FIGURE 9 EBG 3 unit cell (a) Surface current at 5.8 GHz. (b) Reflection phase characteristics. (c) Dispersion diagram. EBG, electromagnetic bandgap.

To customise the EBG array size N , the Ant. 3 is simulated above the $N \times N$ array made of EBG 3 elements and investigated for $N = 5 - 8$. The corresponding S_{11} , S_{12} , AR bandwidth, and gain results are analysed in Figure 10.

The impedance bandwidth, port isolation, AR bandwidth, and gain vary with N . This is because different near-field interactions exist between various EBG arrays and the patch antenna. It is apparent that the Ant. 3 using $N = 7$ provides a high gain of 9.07 dBi, which is higher than using $N = 5, 6$. An impedance bandwidth of 5.26 – 6.1 GHz and AR bandwidth of 5.26 – 5.96 GHz is achieved. The lower gains shown by the $N = 5, 6$ are due to the array sizes, which are small, thus causing excessive backward radiations. Note that a separation of $h_2 = 3$ mm is kept between the Ant. 3 and the EBG structure to facilitate the SubMiniature version A connector placement as shown in Figure 1b. In practice, a styrofoam slab fills this separation h_2 . However, maintaining a uniform gap between two substrates and precise alignment of the patch with respect to the EBG structure becomes challenging, especially in cases of severe bending in real-world environments. These challenges can be mitigated by incorporating flexible adhesives and leveraging advanced manufacturing techniques.

The results indicate that both the $N = 7, 8$ arrays exhibit high gain and good isolation between the two antenna ports as shown in Figures 10b,d, respectively. The increased gain with increasing N is due to low backward radiation at the cost of bigger prototypes. With this trade-off, the $N = 7$ design Ant. 4 with an overall size of $1.12\lambda_0 \times 1.12\lambda_0 \times 0.09\lambda_0$ is chosen as the final layout, where λ_0 corresponds to the lowest frequency in the operative band. The simulated peak gain of 8.57 dBi was achieved by the proposed design (Ant. 4) in the overlapped band of 5.54 – 5.96 GHz. The improvement in port isolation is due to the fact that the surface wave bandgap of EBG

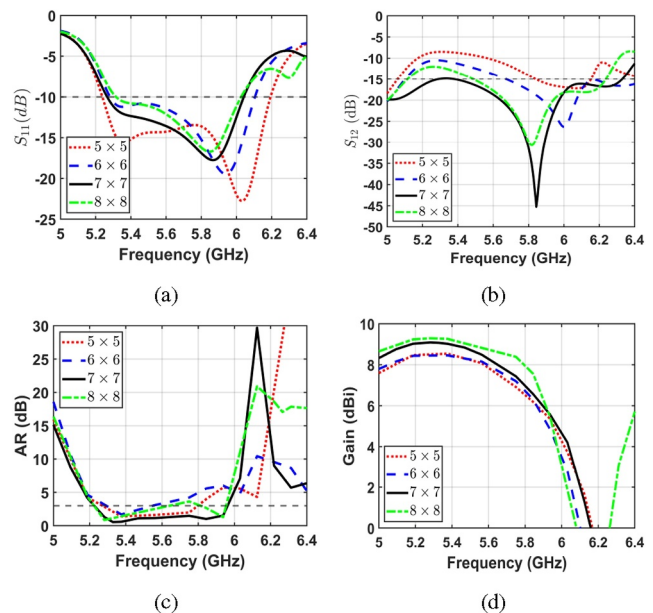


FIGURE 10 Simulated (a) S_{11} . (b) S_{12} . (c) AR. (d) Gain with various N . AR, axial ratio.

coincides with the working frequency of the antenna which results in reduction in mutual coupling [33]. It led to the Ant. 4 with high gain, low-profile, good isolation, and a wider impedance and AR bandwidths covering the 5.8 GHz ISM band (5.725 – 5.875 GHz).

3 | SIMULATION RESULTS

Highlighted in this section are the parametric analysis, radiation mechanism, body loading effects, and bending performance of the proposed design.

3.1 | Parametric analysis

For the proposed design Ant. 4 whose dimensions are defined in Figure 1, a rigorous parametric analysis was conducted through simulations. For brevity, only a few results are analysed such as the key parameters p_1 , l_1 , l_d and l and the corresponding S_{11} , S_{12} , and AR are displayed in Figure 11.

The impedance bandwidth becomes wider with increasing p_1 as presented in Figure 11a. This is because increasing p_1

influences the matching due to EBG, hence shifting the frequency (f_2) towards an upper band, whereas doing the same to the monopole itself (f_1) remains unaffected. Also, port isolation is susceptible to variation in p_1 as shown in Figure 11a. The rationale behind this is that variation in p_1 affects the suppression of surface waves. However, the proper choice of p_1 can be used to tune the AR bandwidth as shown in Figure 11b.

As presented in Figure 11c, matching the monopole at f_1 is affected with increasing l_1 , hence drifting f_1 towards a lower band and is due to the increased current path, whereas f_2 remains almost unaffected. Therefore, enhancement in the impedance bandwidth is obtained. Also, variation in the AR bandwidth is observed with the increase in l_1 as depicted in Figure 11d. This is because the slots i_1 and i_2 contribute to attaining the CP. Furthermore, as depicted in Figure 11c, the port isolation is sensitive to variation in l_1 because it affects the coupled intensity on P_Y when P_X is excited. Best isolation was obtained when $l_1 = 7$ mm.

The varying lengths of the closed-loop feedback structure, l_d of the ring S_q and l improves the impedance bandwidth slightly; however, a better S_{12} is seen in Figure 11e. This is due to the fact that the closed-loop feedback structure contributes positively to the impedance matching as shown in Figure 3a for Ant. 3. Also, variation in l_d and l helps in tailoring the polarisation of the proposed antenna (Ant.4), as displayed in Figure 11f. Note that the DCP of the Ant. 4 can be transformed into dual linear polarisation (DLP) in the band of interest by varying the parameters of the closed-loop feedback structure.

3.2 | Radiation mechanism of the proposed design

Figure 12 depicts the simulated current distributions at 5.8 GHz of the proposed antenna with progressive time phase, that is, $\omega t = 0^\circ$, and 90° to analyse the DCP operation.

The total current direction rotates anticlockwise with the progressive time phase when P_X is excited. Thus, the proposed antenna radiates RHCP from Port 1, as displayed in Figures 12a,b, in the positive z-direction. Similarly, the total current direction rotates clockwise with the progressive phase when P_Y is excited. This results in LHCP radiation from Port 2, as displayed in Figure 12c,d, in the positive z-direction. Hence, the proposed antenna attains the DCP with RHCP and LHCP operations individually from the two ports.

3.3 | Human body loading effects

A $90\text{mm} \times 90\text{mm} \times 33\text{mm}$ planar three-layered human tissue model consisting of skin, fat, and muscle is modelled in HFSS as illustrated in Figure 13. The dielectric characteristics of each tissue and their thicknesses are defined in the figure [36]. The proposed antenna is mounted next to the human phantom at h_0 height above the skin to include the effect of the human outfit.

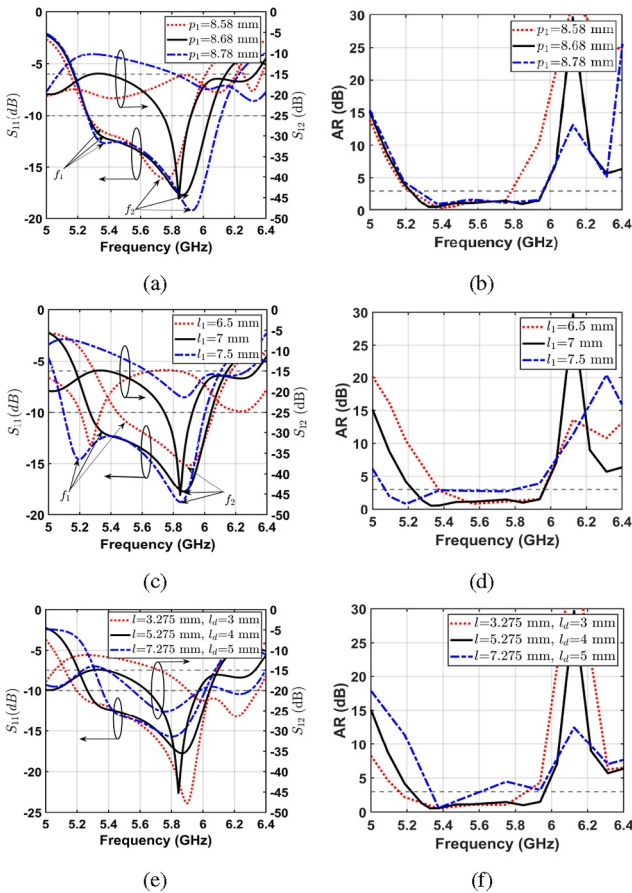


FIGURE 11 Simulated (a) S_{11} and S_{12} . (b) AR with varying lengths p_1 . (c) S_{11} and S_{12} . (d) AR with different lengths l_1 . (e) S_{11} and S_{12} . (f) AR with different lengths l , l_d . AR, axial ratio.

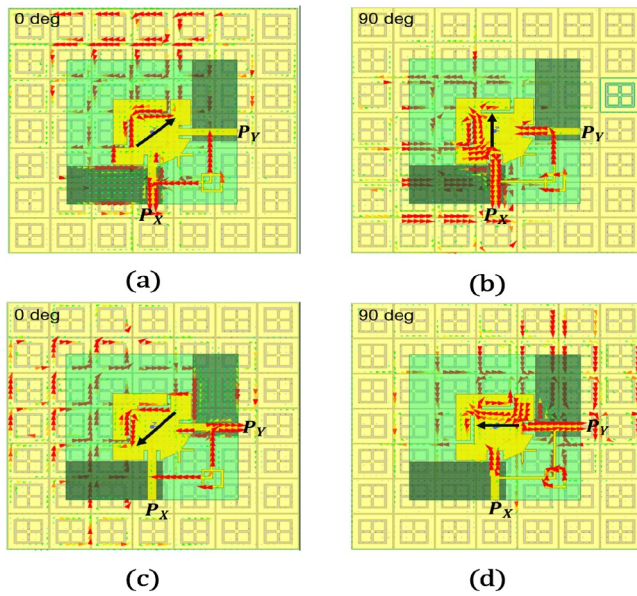


FIGURE 12 Simulated current distributions at 5.8 GHz of the proposed antenna (a)–(b) and (c)–(d), respectively, when P_X and P_Y are excited.

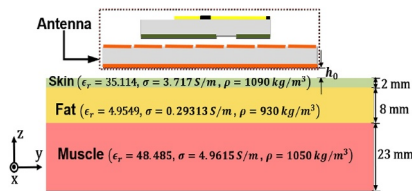


FIGURE 13 Three-layered human phantom with the proposed antenna installed at h_0 height over the skin.

The S_{11} , S_{12} , gain, and AR bandwidth are hardly influenced by altering the h_0 as presented in Figure 14a,b thanks to the EBG array. Additionally, the user's outfits are made of a variety of materials, including polyester, jeans, felt, and cordura, having dielectric characteristics listed in Table 1 [37]. The antenna performance on these materials was investigated and Figures 14c,d show that the performance is barely affected, indicating the robustness of the proposed design.

3.4 | Influence of bending on conformal surface

In consideration of practical wearable scenarios, since the antenna is to be conformed or bent when it is on the user's body, a certain degree of mismatch is inevitable. Consequently, it deteriorates the antenna performance which needs to be investigated under various bending conditions. The proposed antenna is bent along -45° as shown in Figure 15a; therefore, the influence on the P_X and P_Y ports are nearly identical. The bending performance is simulated for S_{11} and S_{12} in Figure 15b and AR and gain in Figure 15c.

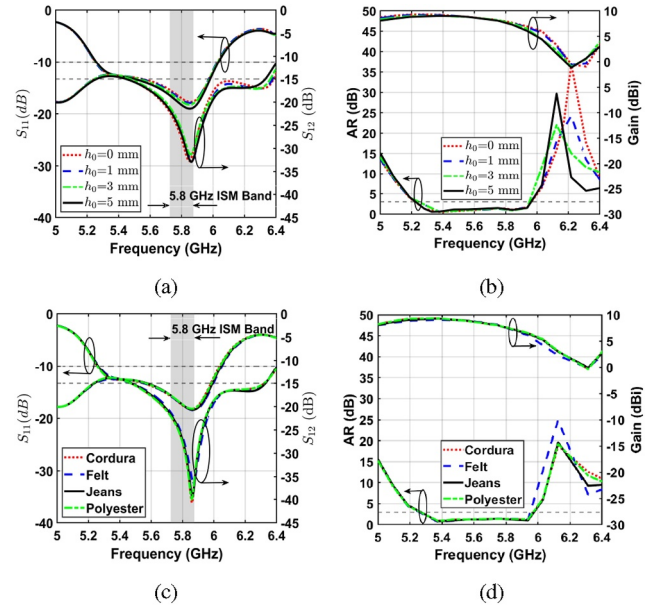


FIGURE 14 Simulated results (a) S_{11} and S_{12} . (b) AR and gain with varying h_0 . (c) S_{11} and S_{12} . (d) AR and gain with different clothing materials. AR, axial ratio.

TABLE 1 Dielectric characteristics of various clothing materials.

	Polyester	Jeans	Felt	Cordura
ϵ_r	1.9	1.6	1.2	1.9
$\tan \delta$	0.0045	0.04	0.02	0.0098

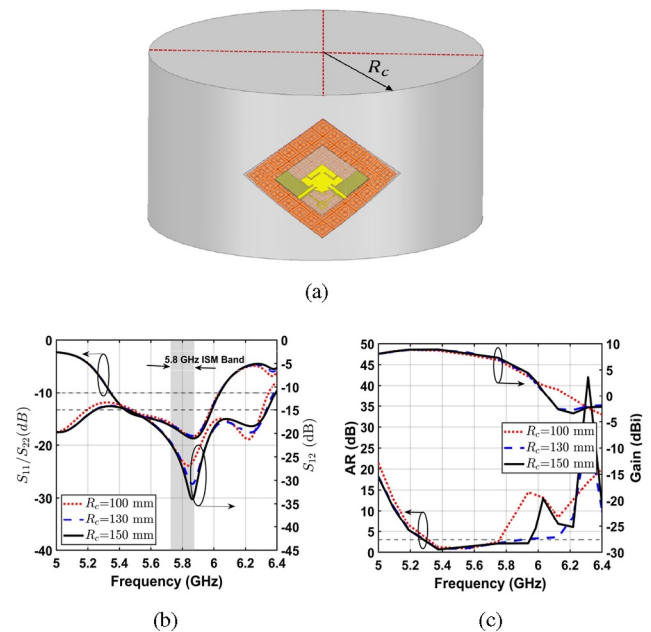


FIGURE 15 The proposed antenna (a) bending along -45° . (b) Simulated S_{11}/S_{22} and S_{12} . (c) Simulated AR and gain. AR, axial ratio.

It is evident from Figure 15b that as the radius of the bend (R_c) decreases from 150 to 130 mm, there is a slight reduction in the impedance bandwidth. However, as illustrated in

Figures 15b,c, a noticeable effect is observed on the dip of the S_{12} and AR bandwidth. This effect is attributed to the bending of the EBG structure, which plays a crucial role in providing the port isolation and enhancing the AR. Also, the antenna maintained its DCP behaviour within the entire 5.8 GHz ISM band as shown in Figure 15c, and there is a tolerance in the AR bandwidth and gain with the increase in bending for $R_c \geq 130$ mm. Whereas, a further decrease in $R_c < 130$ mm results in AR reduction, thus unable to maintain its DCP behaviour in the band of interest.

4 | EXPERIMENTAL VALIDATION OF THE PROPOSED ANTENNA

The proposed antenna was fabricated in Figure 16 and was measured for validation.

First, the antenna performance was examined by mounting it on various body parts as displayed in Figure 17a. The corresponding S_{11}/S_{22} and S_{12} are plotted along with free space measurements in Figures 17b,c. The results show for free space that the measured impedance bandwidth, for which $S_{11} \leq -10$ dB, is 5.35 – 6.10 GHz, hence covering the entire 5.8 GHz ISM band. A measured port isolation of 28 dB in real

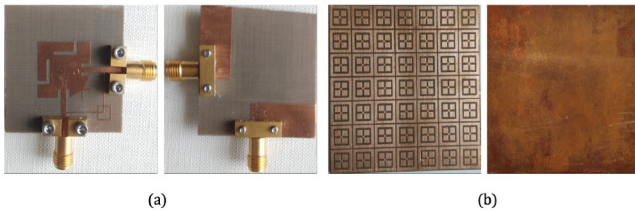


FIGURE 16 Front and back sides of the EBG-integrated antenna prototype (a) monopole. (b) EBG array. EBG, electromagnetic bandgap.

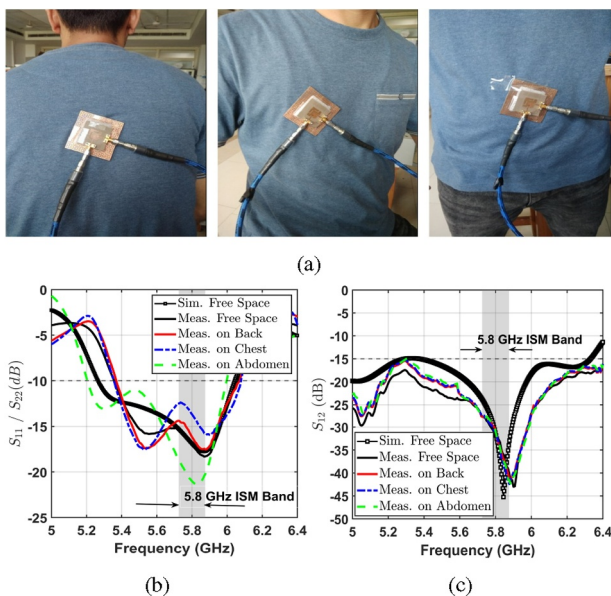


FIGURE 17 Fabricated prototype installed on various body parts (a) back, chest, and abdomen. (b) Measured S_{11}/S_{22} . (c) S_{12} .

scenarios (with potential ~ 34 dB) is achievable within the ISM band. When the proposed design is mounted on various body parts, its impedance performance and port isolation characteristics are comparable with those immediately outlined. This corroborates the observation discussed in Section 3.4.

The antenna radiation characteristics are measured in an anechoic chamber. Figure 18 plots the measured results of the AR and gain under flat (non-bending) conditions which fairly agree with the simulated results. The measured 3 dB AR bandwidth ranges from 5.35 – 6.00 GHz with $|S_{11}|$ below -10 dB. The maximum gain value is measured as 8.76 and 7.53 dBi, within the frequency band from 5.35 – 6.10 to 5.8 GHz ISM band (5.725 – 5.875 GHz), respectively. The minor discrepancies observed in the results are owing to the fabrication and measurement tolerances. The total efficiency of the proposed antenna (simulated) is a $\pm 2\%$, varying between 94% and 98% in the desired band.

Figure 19 presents the measured far-field radiation patterns in xz and yz planes, at 5.8 GHz of the proposed antenna. It is clear from the figure that the RHCP and LHCP are the principal polarisations when P_X and P_Y , respectively, are excited.

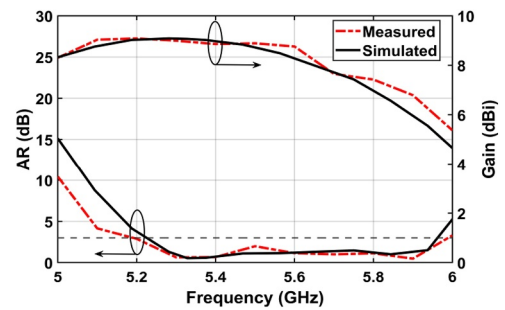


FIGURE 18 AR and gain of the proposed EBG-integrated antenna. AR, axial ratio; EBG, electromagnetic bandgap.

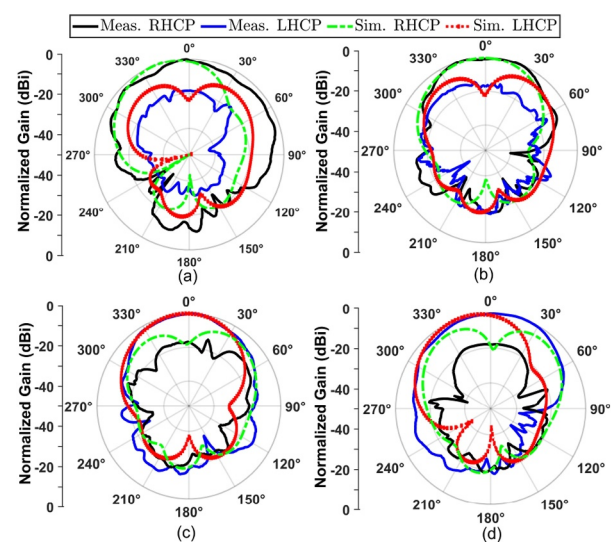


FIGURE 19 Simulated and measured normalised gain pattern results of the EBG-integrated antenna (a) xz plane, P_X is excited. (b) yz plane, P_X is excited. (c) xz plane, P_Y is excited. (d) yz plane, P_Y is excited. EBG, electromagnetic bandgap.

Furthermore, a good cross-polarisation level of above 17 dB is attained, in both states, in the broadside direction, indicating good polarisation discrimination. The radiation pattern tilts from the $+z$ -direction because one of the microstrip feed lines acts as a single shunt stub when the other feed line is excited [14]. This tilting is more apparent at high-frequencies (not shown for brevity) resulting in a reduction of the broadside gain.

5 | SAR ANALYSIS FOR WEARABLE SAFETY

The SAR evaluation setup is displayed in Figure 13, where the proposed antenna is mounted on the human tissue phantom at a gap of h_0 .

The SAR is calculated using $SAR = \frac{\sigma |E|^2}{\rho}$ [27], where ' E ' (V/m) denotes the electric field intensity, ' σ ' (S/m) denotes the human tissue conductivity, and ' ρ ' (kg/m^3) signifies the mass density of the human tissue.

As a benchmark, an input power of 100 mW was selected to determine the amount of the SAR value [2]. As shown in Figure 20, the highest value of the average SAR, over 1 g of

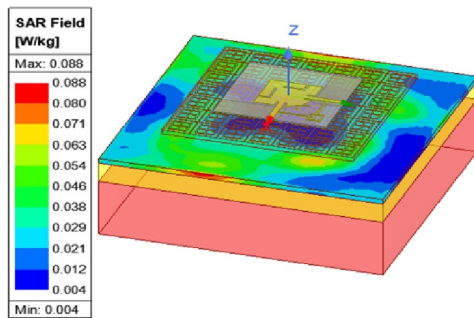


FIGURE 20 Simulated SAR with a distance, h_0 , of 5 mm between the human model and the proposed antenna. SAR, specific absorption rate.

human tissue, is 0.088 W/kg when the separation h_0 is set at 5 mm. Finally, the gap h_0 was varied to inspect its effects on the average SAR. The peak value of SAR is 0.5431 W/kg (over 1 g of tissue) when the proposed antenna was mounted directly ($h_0 = 0$) on the human phantom, and this is well below the allowed limit of 1.6 W/kg. As the spacing h_0 was raised to 5 mm, the average SAR rapidly decreases to 0.088 W/kg. The SAR continues to lower when the distance h_0 is increased further. Hence, the proposed antenna is found to be very safe for wearable applications.

6 | COMPARISON WITH PRIOR WORKS

A detailed comparison between the proposed antenna and other relevant literature is given in Table 2. Compared with the strip-loaded full-duplex antenna in ref. [2], the proposed antenna exhibits DCP, higher port and cross-polarisation isolation, and low SAR. Though the dipole-based MIMO antenna [4] uses a flexible substrate, it suffers from lower gain and high SAR due to bidirectional radiation and poor port and cross-polarisation isolation. In ref. [8], MIMO antenna with good port isolation, in the band of interest, is presented, but it exhibits lower gain due to a lower front-to-back radiation pattern. Moreover, the antenna designs [2, 4, 5, 8] demonstrate LP, and hence they are more prone to polarisation mismatch and multipath interference due to changeable gesture and human body motion. By using DGS structure [19], the antenna shows a very wide impedance bandwidth with DCP characteristics. Nevertheless, the antenna exhibits a lower gain and higher SAR values due to its bidirectional radiation. In ref. [18], unidirectional radiation with good cross-polarisation isolation and DCP characteristics is achieved but more bulky (a bigger prototype). Therefore, compared to the literature, the proposed circulator-like CP antenna offers DCP, high port and cross-polarisation isolation, a more directional radiation pattern, higher gain, lower SAR, and bending tolerance for wearable applications.

TABLE 2 Comparison study of the proposed antenna with various dual-polarised wearable full-duplex and MIMO antennas.

Ref.	Frequency (GHz)	Peak gain (dBi)	Port isolation (dB)	Dual CP	Radiation pattern	Co/Cross-pol. Isolation	SAR (W/kg)
[2]	2.4	7.6	16	No	Unidirectional	12	0.12
[4]	2.4	1.67	12 – 17	No	Bidirectional	$\approx 10^a$	0.44 ^b
[5]	5.8	7	20	No	Omnidirectional	NR	0.29
[18]	5.2 – 6.3	5.8	22	Yes	Unidirectional	17	0.134 ^c
[19]	3.16 – 13	5.7	18	Yes	Bidirectional	$\approx 18^a$	5.434 ^d
[8]	2.4/5.8	2.4/5.2	25	No	Quasi-omnidirectional	$\approx 16^a$	0.024/1.336 ^e
Prop.	5.8	7.53	28 – 34	Yes	Unidirectional	17	0.088

Abbreviations: CP, circularly polarised; NR, not reported.

^aEstimated from the graph.

^b25 mW input power.

^cInput power not mentioned.

^dCalculated for 10 g of tissue at 1 W.

^eOn fat (not on skin) at 200 mW input power.

7 | CONCLUSION

In this work, a circulator-like high gain, unidirectional, DCP wearable antenna with low SAR of 0.088 W/kg for 5.8 GHz ISM band (5.725 – 5.875 GHz) full-duplex WBAN applications was proposed. The DCP full-duplexing was achieved by a closed-loop feedback structure between its orthogonal-ports with enhanced AR bandwidth and good impedance matching. The antenna was backed with a 7×7 EBG array for improved directionality, AR and isolation between the ports. The antenna was simulated and validated experimentally with good agreement between the results. A cross-polarisation level above 17 dB in the broadside direction for both the E- and H-planes indicated good polarisation discrimination. Since the total power at each respective port is maintained and not halved (–3 dB) with a measured port isolation of ~ 28 dB in real scenarios (with potential evidence of ~ 34 dB) within the ISM band, thus a typically cascaded circulator/duplexer can be relieved and left to the digital processing of any self-interference challenge of full duplex systems through digital cancellation techniques, which alleviates the overall costs of RF hardware and eases integration. Future research will concentrate on developing innovative techniques to improve isolation directly at the antenna stage, thereby minimising the need for additional isolation measures in subsequent stages at the transceiver. The measured peak gain in the 5.8 GHz ISM band (5.725 – 5.875 GHz) is 7.53 dBi. Even though DLP as well as DCP can be supported, the closed-loop feedback structure uses a port as Tx (RHCP) and the other one as Rx (LHCP) simultaneously with enhanced AR bandwidth. Without this structure, it would require a circulator/duplexer for DCP full-duplex operation and the associated added insertion losses and/or $\frac{1}{2}$ power (if duplexers) for operation, together with a polarisation misalignment problem that is undesired in wearable WBAN applications.

AUTHOR CONTRIBUTIONS

Ajeet Thakur: Conceptualisation; methodology; software; writing—original draft. **Ashwani Sharma:** Conceptualisation; methodology; resources; supervision; validation; writing—review & editing; project administration. **Ignacio J. Garcia Zuazola:** Conceptualisation; methodology; data curation; investigation; validation; writing—review & editing; supervision; project administration.

ACKNOWLEDGEMENT

This work was supported in part by SERB, Department of Science & Technology, Government of India under Grant CRG/2022/007257.

CONFLICT OF INTEREST STATEMENT

The authors declare no conflicts of interest.

DATA AVAILABILITY STATEMENT

The data that support the findings of this study are available from the corresponding author upon reasonable request.

ORCID

Ajeet Thakur  <https://orcid.org/0009-0005-1381-2723>

Ignacio J. Garcia Zuazola  <https://orcid.org/0000-0001-8580-0194>

REFERENCES

- Fields, R.E.: Evaluating compliance with FCC guidelines for human exposure to radiofrequency electromagnetic fields. *OET Bull.* 65(10) (1997)
- Mao, C.X., et al.: Low-profile strip-loaded textile antenna with enhanced bandwidth and isolation for full-duplex wearable applications. *IEEE Trans. Antenn. Propag.* 68(9), 6527–6537 (2020). <https://doi.org/10.1109/tap.2020.2989862>
- Mao, C.X., Gao, S., Wang, Y.: Dual-band full-duplex Tx/Rx antennas for vehicular communications. *IEEE Trans. Veh. Technol.* 67(5), 4059–4070 (2018). <https://doi.org/10.1109/tvt.2017.2789250>
- Li, H., et al.: Design of compact single-layer textile mimo antenna for wearable applications. *IEEE Trans. Antenn. Propag.* 66(6), 3136–3141 (2018). <https://doi.org/10.1109/tap.2018.2811844>
- Mao, C.X., et al.: Dual-polarized embroidered textile armband antenna array with omnidirectional radiation for on-/off-body wearable applications. *IEEE Trans. Antenn. Propag.* 68(4), 2575–2584 (2020). <https://doi.org/10.1109/tap.2019.2951517>
- Lee, H., Tak, J., Choi, J.: Wearable antenna integrated into military berets for indoor/outdoor positioning system. *IEEE Antenn. Wireless Propag. Lett.* 16, 1919–1922 (2017). <https://doi.org/10.1109/lawp.2017.2688400>
- Mendes, C., Peixeiro, C.: A dual-mode single-band wearable microstrip antenna for body area networks. *IEEE Antenn. Wireless Propag. Lett.* 16, 3055–3058 (2017). <https://doi.org/10.1109/lawp.2017.2760142>
- Yang, L., et al.: Dual-band flexible MIMO antenna with self-isolation enhancement structure for wearable applications. *Chin. J. Electron.* 32(4), 692–702 (2023). <https://doi.org/10.23919/cje.2021.00.293>
- Yazdandoost, K.Y., Miura, R.: Antenna polarization mismatch in ban communications. In: *IEEE MTT-S International Microwave Workshop Series on RF and Wireless Technologies for Biomedical and Healthcare Applications*, pp. 1–3. (IMWS-BIO) (2013)
- Cui, P.F., et al.: Off-body spatial diversity reception using circular and linear polarization: measurement and modeling. *IEEE Commun. Lett.* 22(1), 209–212 (2018). <https://doi.org/10.1109/lcomm.2017.2762324>
- Gao, S., Sambell, A., Zhong, S.S.: Polarization-agile antennas. *IEEE Antenn. Propag. Mag.* 48(3), 28–37 (2006). <https://doi.org/10.1109/map.2006.1703396>
- Ds, C., Karthikeyan, S.S.: A novel broadband dual circularly polarized microstrip-fed monopole antenna. *IEEE Trans. Antenn. Propag.* 65(3), 1410–1415 (2017). <https://doi.org/10.1109/tap.2016.2647705>
- Xu, R., et al.: A design of u-shaped slot antenna with broadband dual circularly polarized radiation. *IEEE Trans. Antenn. Propag.* 65(6), 3217–3220 (2017). <https://doi.org/10.1109/tap.2017.2689069>
- Saini, R.K., Dwari, S.: A broadband dual circularly polarized square slot antenna. *IEEE Trans. Antenn. Propag.* 64(1), 290–294 (2016). <https://doi.org/10.1109/tap.2015.2496118>
- Chen, W., et al.: Developing wideband dual-circularly polarized antenna with simple feeds using magnetoelectric dipoles. *IEEE Antenn. Wireless Propag. Lett.* 19(6), 1037–1041 (2020). <https://doi.org/10.1109/lawp.2020.2988560>
- Tran, H.H., Nguyen Trong, N., Park, H.C.: A compact dual circularly polarized antenna with wideband operation and high isolation. *IEEE Access* 8, 182959–182965 (2020). <https://doi.org/10.1109/access.2020.3022845>
- Jamal, M.Y., Li, M., Yeung, K.L.: Isolation enhancement of closely packed dual circularly polarized mimo antenna using hybrid technique. *IEEE Access* 8, 11241–11247 (2020). <https://doi.org/10.1109/access.2020.2964902>
- Ullah, U., Mabrouk, I.B., Koziel, S.: Enhanced-performance circularly polarized MIMO antenna with polarization/pattern diversity. *IEEE*

- Access 8, 11887–11895 (2020). <https://doi.org/10.1109/access.2020.2966052>
19. Kumar, S., et al.: Wideband circularly polarized textile MIMO antenna for wearable applications. *IEEE Access* 9, 108601–108613 (2021). <https://doi.org/10.1109/access.2021.3101441>
 20. Kumar, S., et al.: Compact dual circularly-polarized quad-element MIMO/diversity antenna for sub-6 GHz communication systems. *Sensors* 22(24), 9827 (2022). <https://doi.org/10.3390/s22249827>
 21. Mousavirazi, Z., et al.: A low-profile and low-cost dual circularly polarized patch antenna. *Prog. Electromagnetics Res. Lett.*, 107 (2022)
 22. Li, J.F., et al.: A dual-circularly-polarized wideband dipole antenna with stable axial-ratio and half-power beamwidths. *IEEE Antenn. Wireless Propag. Lett.* 22(7), 1701–1705 (2023). <https://doi.org/10.1109/lawp.2023.3260642>
 23. Ta, S.X., et al.: Wideband dual-circularly polarized antennas using aperture-coupled stacked patches and single-section hybrid coupler. *IEEE Access* 10, 21883–21891 (2022). <https://doi.org/10.1109/access.2022.3155120>
 24. Simorangkir, R.B., Kiourti, A., Esselle, K.P.: Uwb wearable antenna with a full ground plane based on pdms-embedded conductive fabric. *IEEE Antenn. Wireless Propag. Lett.* 17(3), 493–496 (2018). <https://doi.org/10.1109/lawp.2018.2797251>
 25. Augustine, R., et al.: Polymeric ferrite sheets for sar reduction of wearable antennas. *Electron. Lett.* 46(3), 197 (2010). <https://doi.org/10.1049/el.2010.3246>
 26. Haridim, M.: Use of rod reflectors for sar reduction in human head. *IEEE Trans. Electromagn. C.* 58(1), 40–46 (2016). <https://doi.org/10.1109/temc.2015.2500818>
 27. Elsheakh, D.M.N., Soliman, A.M., Abdallah, E.A.: Low specific absorption rate hexa-band coplanar waveguide-fed planar inverted-f antenna with independent resonant frequency control for wireless communication applications. *IET Microw., Antennas Propag.* 8(4), 207–216 (2014). <https://doi.org/10.1049/iet-map.2013.0100>
 28. Ashyap, A.Y.I., et al.: Compact and low-profile textile ebg-based antenna for wearable medical applications. *IEEE Antenn. Wireless Propag. Lett.* 16, 2550–2553 (2017). <https://doi.org/10.1109/lawp.2017.2732355>
 29. Yan, S., Soh, P.J., Vandenbosch, G.A.E.: Low-profile dual-band textile antenna with artificial magnetic conductor plane. *IEEE Trans. Antenn. Propag.* 62(12), 6487–6490 (2014). <https://doi.org/10.1109/tap.2014.2359194>
 30. Alemaryeen, A., Noghianian, S.: Crumpling effects and specific absorption rates of flexible amc integrated antennas. *IET Microw., Antennas Propag.* 12(4), 627–635 (2018). <https://doi.org/10.1049/iet-map.2017.0652>
 31. Ali, U., et al.: Design and sar analysis of wearable antenna on various parts of human body, using conventional and artificial ground planes. *J. Electr. Eng. Tech.* 12(1), 317–328 (2017). <https://doi.org/10.5370/jeet.2017.12.1.317>
 32. Zhang, K., Soh, P.J., Yan, S.: Meta-wearable antennas—a review of metamaterial based antennas in wireless body area networks. *Materials* 14(1), 149 (2020). <https://doi.org/10.3390/ma14010149>
 33. Rajo Iglesias, E., Quevedo Teruel, O., Inclan Sanchez, L.: Mutual coupling reduction in patch antenna arrays by using a planar ebg structure and a multilayer dielectric substrate. *IEEE Trans. Antenn. Propag.* 56(6), 1648–1655 (2008). <https://doi.org/10.1109/tap.2008.923306>
 34. Raad, H.R., et al.: Flexible and compact AMC based antenna for telemedicine applications. *IEEE Trans. antennas propagation* 61(2), 524–531 (2012)
 35. Chaouche, Y.B., et al.: A wearable circularly polarized antenna backed by amc reflector for WBAN communications. *IEEE Access* 10, 12838–12852 (2022). <https://doi.org/10.1109/access.2022.3146386>
 36. ElAtrash, M., Abdalla, M.A., Elhennawy, H.M.: A wearable dual-band low profile high gain low SAR antenna AMC-backed for WBAN applications. *IEEE Trans. Antenn. Propag.* 67(10), 6378–6388 (2019). <https://doi.org/10.1109/tap.2019.2923058>
 37. Salvado, R., et al.: Textile materials for the design of wearable antennas: a survey. *Sensors* 12(11), 15841–15857 (2012). <https://doi.org/10.3390/s121115841>

How to cite this article: Thakur, A., Sharma, A., Zuazola, I.J.G.: A wearable circulator-like circularly polarised antenna for full-duplex wireless body area network applications. *IET Microw. Antennas Propag.* 1–11 (2024). <https://doi.org/10.1049/mia2.12507>